

Article

Constraints on Petrogenesis and Fe Fertility of Intrusive Complexes in the Han–Xing Region, North China Craton from Apatite Geochemistry

Xian Liang ^{1,2}, Fangyue Wang ^{1,2,*}, Juquan Zhang ^{3,4,*}, Long Zhang ^{1,2}, Junwu Zhang ⁵ and Jingui Wang ⁶

¹ Ore Deposit and Exploration Center, School of Resources and Environmental Engineering, Hefei University of Technology, Hefei 230009, China

² Anhui Province Engineering Research Center for Mineral Resources and Mine Environments, Hefei 230009, China

³ College of Earth Sciences, Hebei GEO University, 136 Huaiaidong Road, Shijiazhuang 050031, China

⁴ Hebei Key Laboratory of Strategic Critical Mineral Resources, Hebei GEO University, Shijiazhuang 050031, China

⁵ Mongolia Zhengyuan Co., Ltd., Jinan 250101, China

⁶ Regional Geological Survey Institute of Hebei Province, Langfang 065000, China

* Correspondence: fywang@hfut.edu.cn (F.W.); juquan1983@163.com (J.Z.)

Abstract: The Han–Xing (Handan–Xingtai) region is famous for its endowment of skarn iron deposits in China. These deposits are mainly spatially and genetically associated with diorite rocks, but these rocks show different Fe ore potential. Major and trace elements composition of apatite from the Kuangshan and Fushan diorite complexes were investigated to explore the potential of apatite as a proxy of petrogenesis and Fe fertility of these rocks. All the investigated apatite grains are identified as fluorapatite, which is typical for magmatic apatite. The Sr, Y, Mn, and Heavy Rare Earth Elements (HREE) contents of apatite in the Kuangshan diorite complex are positively correlated with the increase of melt SiO₂ content compared to that in the Fushan diorite complex. Apatite geochemistry indicates that magmas of the Fushan complex mainly experienced the fractional crystallization of hornblende in the deep crustal reservoirs, whereas the Kuangshan complex has experienced the fractional crystallization of hornblende in the deep and the shallow plagioclase fractional crystallization. The F, Cl and S content of the Kuangshan complex estimated by apatite volatile (F = 2632 ppm, Cl = 4100 ppm, SO₃ = 140 ppm) is significantly higher than that of the Fushan complex (F = 2488 ppm, Cl = 3400 ppm, SO₃ = 90 ppm). The Eu, Ce anomalies, Mn, and SO₃ contents of apatite show that both of the two complexes have higher oxygen fugacity (Δ FMQ), but the oxygen fugacity of the Kuangshan complex calculated by Mn and SO₃ content (Δ FMQ + 2.41) is higher than that of the Fushan complex (Δ FMQ + 1.77), which may also be one of the reasons for the great difference in ore-forming scale between the two complexes. Our results suggest that the high volatile contents and oxidation states of magma estimated by apatite, as well as the lower Sr/Y in apatite reflect favorable conditions for skarn iron mineralization. Therefore, our study shows that magmatic apatite geochemistry may be a useful tool to distinguish the Fe fertility of plutonic rocks related to skarn deposits.

Keywords: apatite; Han–Xing iron deposits; magma evolution; Fe fertility; diorite complexes



Citation: Liang, X.; Wang, F.; Zhang, J.; Zhang, L.; Zhang, J.; Wang, J. Constraints on Petrogenesis and Fe Fertility of Intrusive Complexes in the Han–Xing Region, North China Craton from Apatite Geochemistry. *Minerals* **2023**, *13*, 469. <https://doi.org/10.3390/min13040469>

Academic Editor: Mauricio Calderón

Received: 18 December 2022

Revised: 21 March 2023

Accepted: 23 March 2023

Published: 26 March 2023



Copyright: © 2023 by the authors. Licensee MDPI, Basel, Switzerland. This article is an open access article distributed under the terms and conditions of the Creative Commons Attribution (CC BY) license (<https://creativecommons.org/licenses/by/4.0/>).

1. Introduction

Apatite is a common accessory mineral in igneous and metamorphic rocks and is generally resistant to hydrothermal alteration and weathering [1,2]. It can incorporate a significant amount of volatile components (Cl, F, and SO₃) and trace elements, such as rare earth elements (REE), Y, Mn, Si, Sr, Th, and U [3–6]. Apatite is useful in deciphering key parameters of a melt during magma evolution [7–9], and volatile contents [8–16], which

can be evaluated in terms of redox state [2,17–26]. Apatite can act as a powerful tool for ore exploration, such as porphyry Cu-Mo-Au deposits [2,14,18,22,27–29], skarn Pb-Zn-W-Sn deposits [2,18], and granite-related U deposits [17]. However, apatite as an indicator of the ore potential of intrusive complexes related to skarn Fe deposits has not yet been evaluated.

The Han–Xing region is one of the most important skarn iron ore producers in eastern China [30,31]. In this region, skarn iron deposits are spatially related to several diorite complexes [32–34]. However, different diorite complexes have distinct Fe ore potentials. For example, eight Fe deposits with intermediate or small sizes have been found in the Fushan complex, while more than twenty-six Fe deposits, including three large- and four intermediate-sized ones, are spatially within the Kuangshan complex [31]. The factors that result in the difference in Fe fertility of the two complexes are still poorly understood. Previous studies have shown that geochemical characteristics of hornblende, plagioclase, clinopyroxene, and zircon in diorite complexes in the Han–Xing region can be used as an indicator of Fe fertility of diorite rocks related to skarn Fe deposits [31,32,34–38]. Few studies have focused on the geochemical characteristics of apatite in these diorite complexes, and whether it can be an indicator of Fe fertility of these rocks has not been explored.

Iron is one of the main elements in the Earth’s crust. At present, iron deposits have been found in many kinds of lithologies around the world [39–45]. The formation of skarn iron ore is controlled by systematic variables such as the depth magma evolution, shallow assimilation of carbonate-rich and/or gypsolyte, the alteration, the oxygen fugacity of crystallizing magmas, and variations of volatiles, temperature, and pressure.

In this study, the Fushan complex and the Kuangshan complex in the Han–Xing region were taken as two integral metallogenic systems. The in situ major and trace element compositions of apatite in both plutonic complexes were studied, and the characteristics of apatite geochemistry, oxygen fugacity, and volatiles were compared comprehensively, to analyze the favorable metallogenic conditions, which can be used as a guide for mineral exploration.

2. Geological Setting

The Han–Xing region, located in the southern part of the Taihang Mountains, hosts a large number of Mesozoic high-Mg diorite-related skarn-type iron deposits [33,34,46–51]. It covers an area of ~350 km². The Mesozoic magmatism in this region might be related to the destruction of the North China Craton [34,52–57] (Figure 1a) and the subduction of the Paleo-Pacific Plate [52,54]. This region hosts skarn iron deposits that are characterized by high grades of magnetite, with identified iron resources of ca. one billion tonnes. The fault zone in this region is composed of a series of NS- and NE-trending faults, together with EW-trending hidden faults (Figure 1b). The strata in this area are mainly evaporites and limestones of the Middle Ordovician Series. The formation is inclined to the NEE, with a dip Angle of 5–30°. Magmatic rocks mainly include gabbro diorite, hornblende diorite, diorite, diorite porphyrite, monzonite, and syenite [30,34,53,55] (Figure 1b). These rocks were emplaced during 125 Ma–135 Ma [35,48,53].

In this region, skarn Fe deposits are spatially and genetically related to the Qicun, Kuangshan, Wu’an, Guzhen, and Fushan diorite complexes, while the Hongshan complex is barren. Some comparative studies of the whole-rock and major-mineral geochemistry of ore-bearing and barren complexes in the Han–Xing region [32,35,36] pointed out that the ore-bearing and barren complexes display similar geochemical characteristics. They originated from an enriched mantle source, but experienced distinct magmatic processes. The zircon Hf-O and whole-rock Sr-Nd isotopes, as well as their trace element data, indicate that the parental magma of the ore-bearing complex was a mixture of melts that were derived from the enriched lithospheric mantle and ancient lower continental crust, whereas the barren complex was most likely generated by partial melting of the enriched lithospheric mantle [32,35,36]. The lower crustal materials may have played key roles in iron mineralization [35,36]. The ore-bearing complexes in the Han–Xing region have low magma temperatures [35,36]. High oxidation states and water contents have been consid-

ered as the key factors that led to the iron mineralization [32,35–37]. Dolomitic limestone promoted iron mineralization from ore-forming fluids with high fO_2 [34]. Previous mineral explorations and studies show that different ore-bearing diorite complexes may have distinct Fe fertility [31]. For example, three large-, four intermediate-, and nineteen small-sized skarn iron deposits are spatially related to the Kuangshan diorite complex, while only four intermediate- and small-sized ones have been found in the Fushan diorite complex.

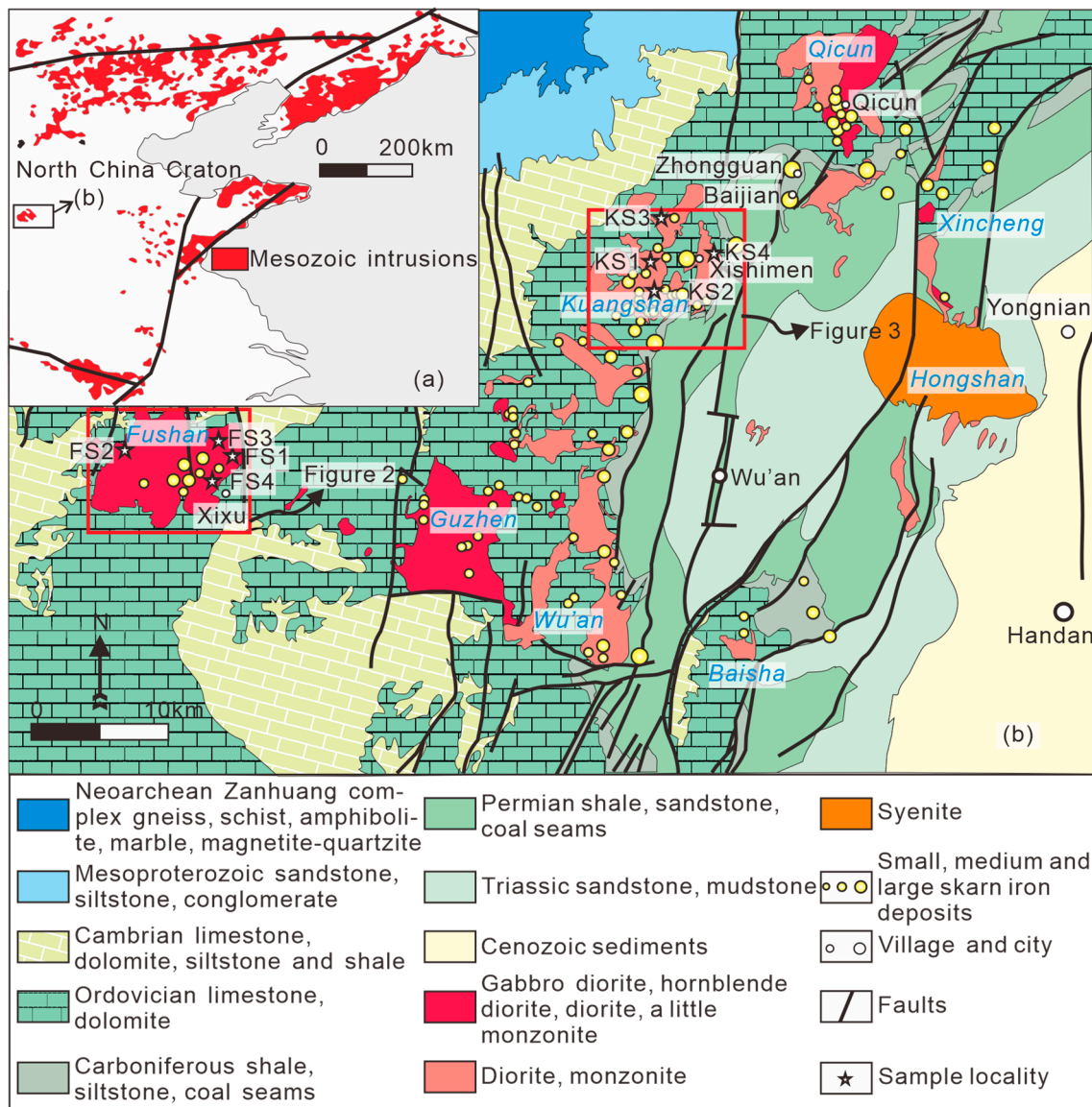


Figure 1. (a) Geological map of the North China Craton (revised from [52]); (b) Geological map of the Han–Xing region (revised from [34]).

2.1. Geology of the Fushan Complex and Related Fe Deposits

The Fushan diorite complex is composed of porphyritic hornblende diorite, hornblende diorite, diorite, monzonite, and minor syenite, with an exposed area of about 80 km² [55] (Figure 2). There are four intermediate-sized iron deposits and four small-sized iron deposits in the Fushan complex. Skarnization was developed in the contact zone between limestone and the complexes, and skarn mainly includes garnet, vesuvianite, diopside, epidote, and actinolite. Most of the magnetite orebodies occur within the contact zones. Zircon U–Pb dating indicates that the Fushan complex were emplaced at 123–131 Ma [31,48,55,58–62].

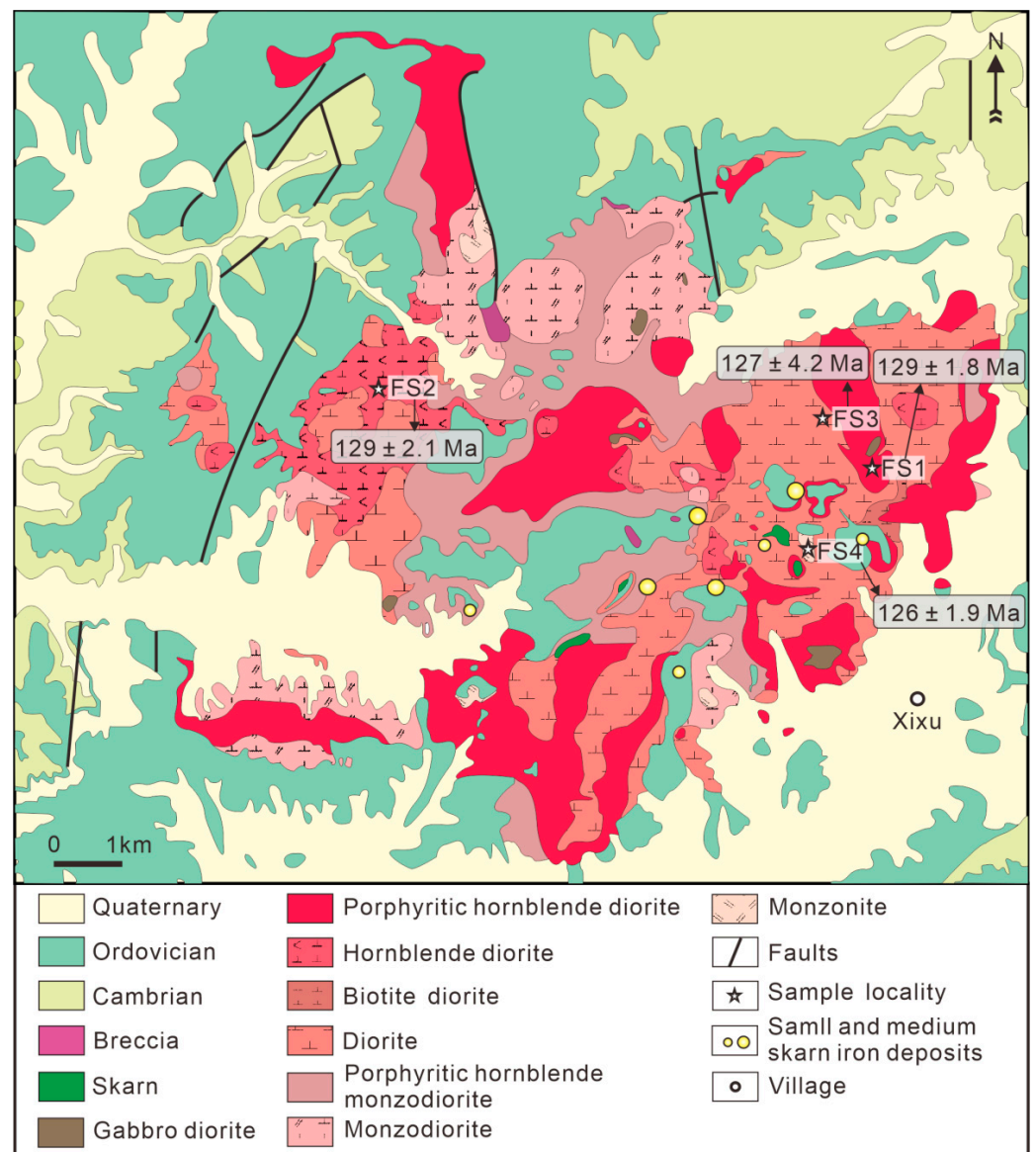


Figure 2. Geological map of the Fushan complex (modified after [55]). Age data are from [58].

2.2. Geology of the Kuangshan Complex and Related Fe Deposits

The Kuangshan complex is composed of monzonite, porphyry monzonite, monzodiorite, and syenodiorite, with an exposed region of about 35 km² (Figure 3). Three large-, four intermediate-, and nineteen small-sized skarn iron deposits are related to the Kuangshan complex. Zircon U-Pb dating indicates that the Kuangshan complex were emplaced during 127–133 Ma [32,40,48,58,62], and the phlogopite ⁴⁰Ar–³⁹Ar isotopic age indicates that the formation ages of the Xishimen iron deposit is 133Ma [63].

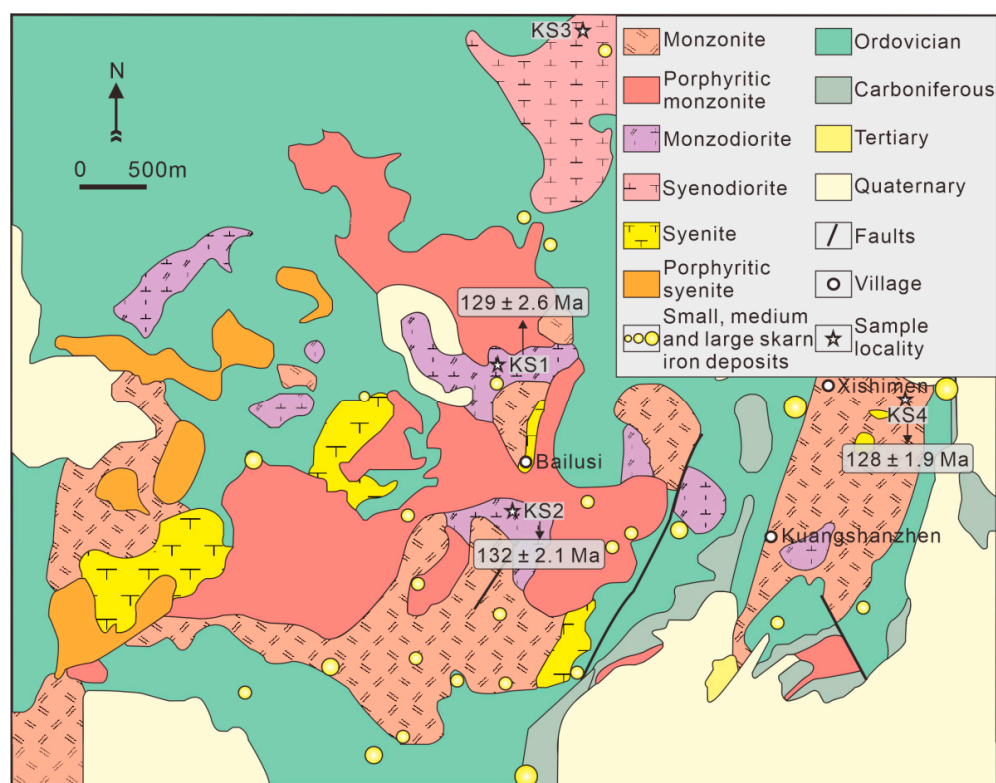


Figure 3. Geological map of the Kuangshan complex (modified after [64]). Age data are from [58].

3. Sampling and Analytical Methods

3.1. Sample Descriptions

The samples collected from the Fushan and Kuangshan complexes are described in Table 1. Four representative samples were collected from the Fushan complex, including porphyritic hornblende diorite (FS1), hornblende diorite (FS2), diorite (FS3), and monzonite (FS4) (Figure 4a–f). Diorite constitutes the main body of the Fushan complex and hornblende diorite occurs as enclaves enclosed in that rock (Figure 4a). Syenite appears as veins within diorite (Figure 4a), and hornblende diorite occur in diorite (Figure 4b). The porphyritic hornblende diorite shows a dark gray color and is mainly composed of plagioclase (60 vol.%), amphibole (35 vol.%), clinopyroxene (5 vol.%), and minor quartz (Figure 4c). The accessory minerals include apatite, magnetite, zircon, and titanite. Hornblende diorite is grey-black in color and is mainly composed of plagioclase (60 vol.%), amphibole (40 vol.%), and a small amount of quartz (Figure 4d,g). The accessory minerals are apatite, magnetite, and zircon. Diorite is gray and is mainly composed of plagioclase (75 vol.%), amphibole (20 vol.%), and a small amount of quartz (Figure 4e,h). The accessory minerals are apatite, magnetite, and zircon. The monzonite shows a light gray color and is mainly composed of plagioclase (50 vol.%), amphibole (15 vol.%), and alkaline feldspar (35 vol.%), and a small amount of quartz (Figure 4f,i). The accessory minerals are apatite, magnetite, zircon, and titanite. Here, the analyzed apatites are enclosed in fresh amphibole, indicating its magmatic origin (Figure 4j–o).

Four representative samples were collected from the Kuangshan complex, including diorite (KS1), quartz diorite (KS2), syenodiorite (KS3), and quartz monzonite (KS4) (Figure 5a–d). Diorite is grey and is mainly composed of plagioclase (65 vol.%), amphibole (30 vol.%), and a small amount of K-feldspar (5 vol.%) (Figure 5a,e,i). The accessory minerals are apatite, magnetite, zircon, and titanite. The quartz diorite shows a gray color and is mainly composed of plagioclase (70 vol.%), amphibole (20 vol.%), and a small amount of quartz (10 vol.%) (Figure 5b,f,j). The accessory minerals are apatite, magnetite, zircon, and titanite. Syenodiorite is gray and is mainly composed of plagioclase (60 vol.%), amphibole

(10 vol.%), and K-feldspar (30 vol.%) (Figure 5c,g,k). The accessory minerals are apatite, magnetite, zircon, and titanite. The quartz monzonite shows a gray color and is mainly composed of plagioclase (40 vol.%), amphibole (10 vol.%), and K-feldspar (40 vol.%), and an amount of quartz (10 vol.%) (Figure 5d,h,l). The accessory minerals include apatite, magnetite, zircon, and titanite. Apatite in these rocks mainly occurs within amphibole (Figure 5i–l).

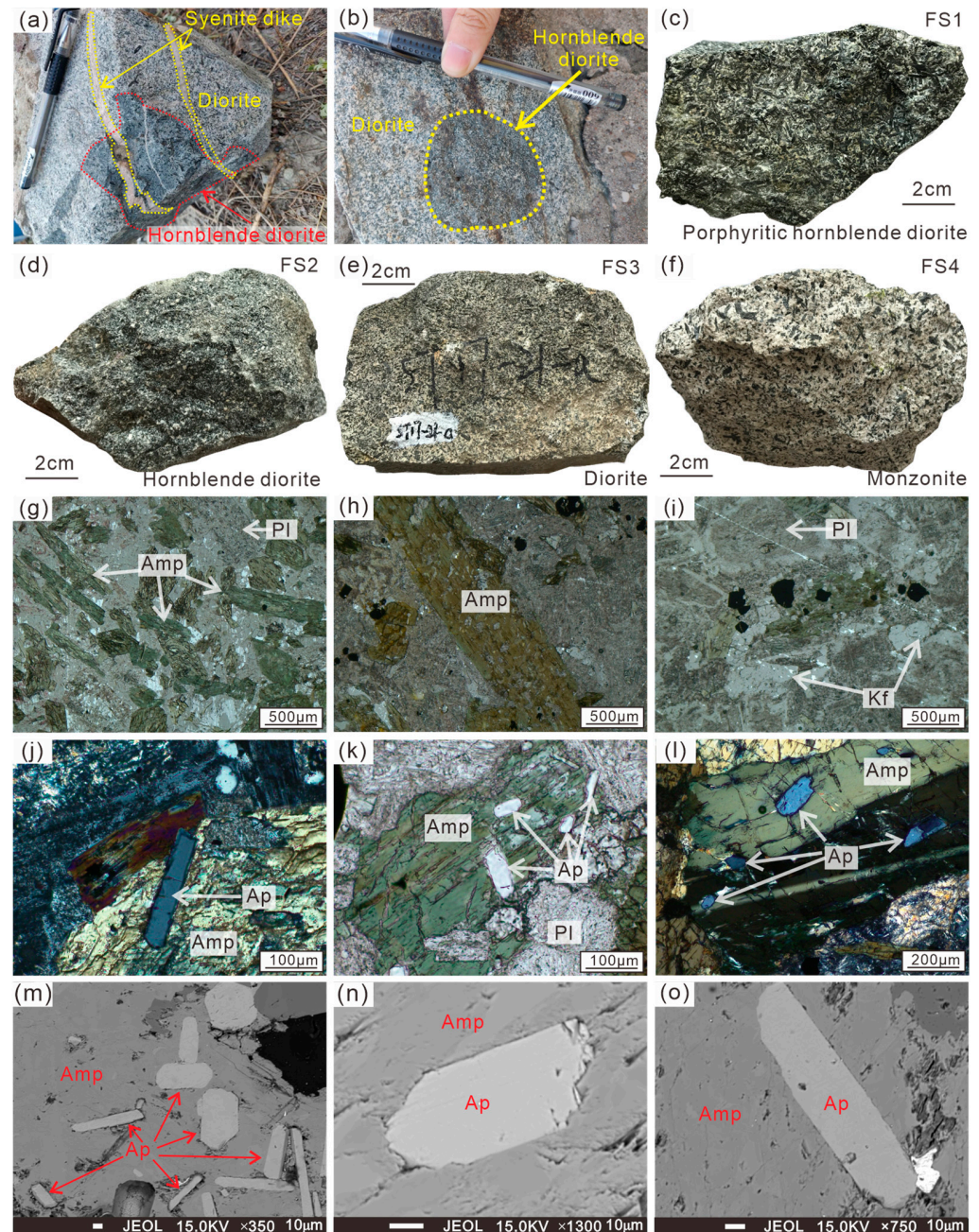


Figure 4. Sample features of the Fushan complex, (a) Hornblende diorite inclusions in diorite, diorite cut by syenite dikes; (b) Hornblende diorite occurs as enclaves enclosed in diorite; (c) Porphyritic hornblende diorite (FS1); (d) Hornblende diorite (FS2); (e) Diorite (FS3); (f) Monzonite (FS4); (g) Hornblende diorite (FS2), under plane-polarized light; (h) Diorite (FS3), under plane-polarized light; (i) Monzonite (FS4), under plane-polarized light; (j–l) Apatite coexisting with amphibole in some samples; (m–o) Apatite coexisting with amphibole in backscattering image. Mineral abbreviations: Amp = amphibole, Pl = plagioclase, Qtz = quartz, Cpx = clinopyroxene, Kf = K-feldspar, Sph = sphen (titanite), Ap = apatite, Mag = magnetite.

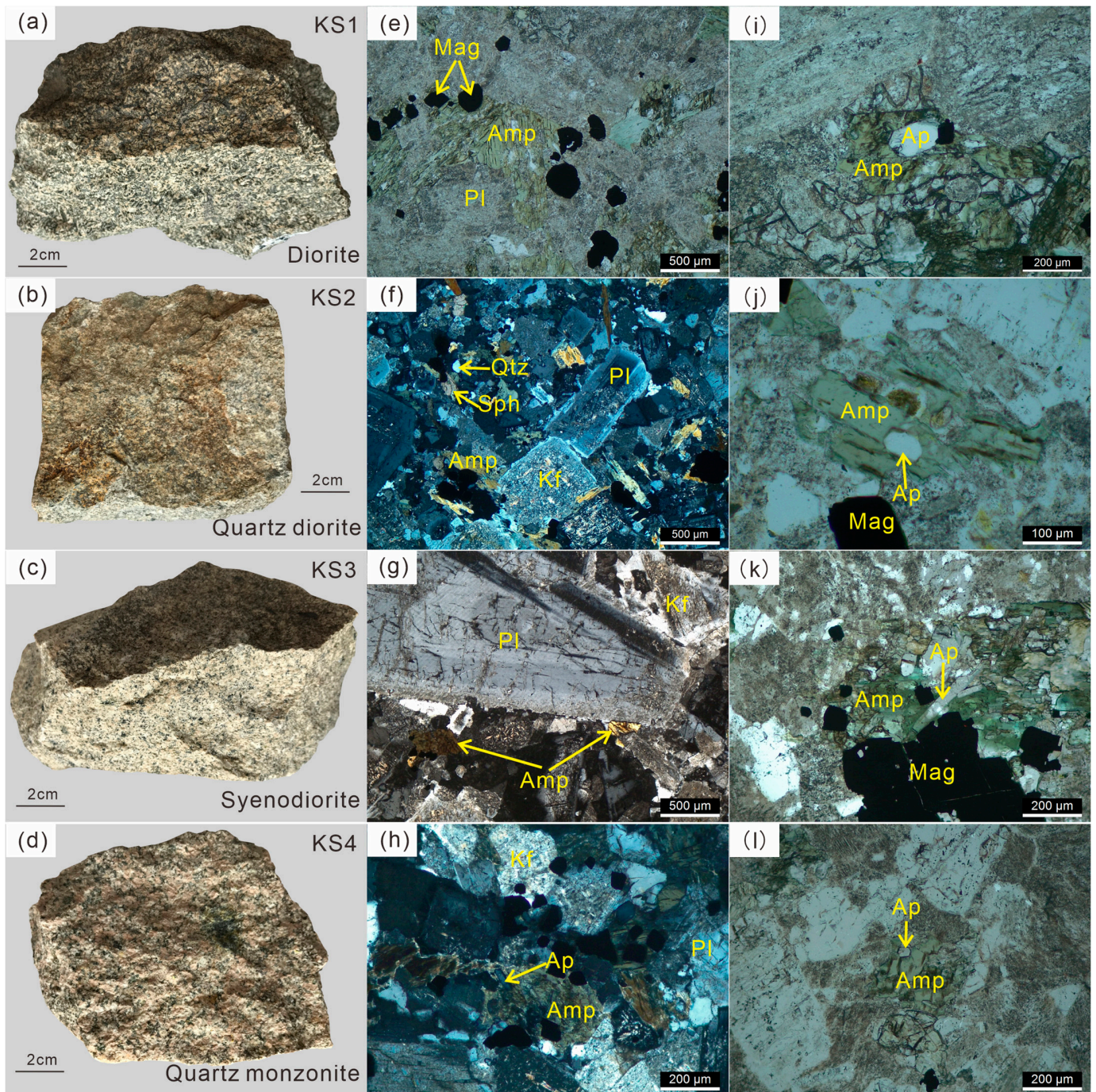


Figure 5. Sample features of the Kuangshan complex. (a) Diorite (KS1); (b) Quartz diorite (KS2); (c) Syenodiorite (KS3); (d) Quartz monzonite (KS4); (e) Diorite (KS1), under plane-polarized light; (f) Quartz diorite (KS2), under cross-polarized light; (g) Syenodiorite (KS3), under cross-polarized light; (h) Quartz monzonite (KS4), under cross-polarized light; (i–l) Apatite coexisting with amphibole in some samples.

Table 1. Comparison of the sample features in the Fushan and Kuangshan complexes.

Sample No.	Complex	Lithology	Texture	Main Mineral	Accessory Mineral	U-Pb Dating
FS1	Fushan	Porphyritic hornblende diorite	Porphyritic texture	Pl(60%) + Amp(35%) + Cpx(5%)	Ap + Mag + Zrn + Sph	129 ± 1.8 Ma
FS2	Fushan	Hornblende diorite	Hypidiomorphic-granular texture	Pl(60%) + Amp(40%)	Ap + Mag + Zrn	129 ± 2.1 Ma
FS3	Fushan	Diorite	Hypidiomorphic-granular texture	Pl(75%) + Amp(25%)	Ap + Mag + Zrn	127 ± 4.2 Ma
FS4	Fushan	Monzonite	Hypidiomorphic-granular texture	Pl(50%) + Amp(15%) + Kf(35%)	Ap + Mag + Zrn + Sph	126 ± 1.9 Ma
KS1	Kuangshan	Diorite	Medium-fine grained texture	Pl(65%) + Amp(30%) + Kf(5%)	Ap + Mag + Zrn + Sph	129 ± 2.6 Ma
KS2	Kuangshan	Quartz diorite	Medium-fine grained texture	Pl(70%) + Amp(20%) + Q(10%)	Ap + Mag + Zrn + Sph	132 ± 2.1 Ma
KS3	Kuangshan	Syenodiorite	Medium-fine grained texture	Pl(60%) + Amp(10%) + Kf(30%)	Ap + Mag + Zrn + Sph	–
KS4	Kuangshan	Quartz monzonite	Medium-coarse grained texture	Pl(40%) + Amp(10%) + Kf(40%) + Q(10%)	Ap + Mag + Zrn + Sph	128 ± 1.9 Ma

3.2. Analytical Methods

Apatite from thin sections of samples from the Fushan and Kuangshan complexes were analyzed to determine their major and trace element compositions. Major elements measurements in apatite were performed using a JEOL JXA-8230 electron probe micro-analyzer (EPMA) at the Hebei GEO University, Shijiazhuang, China. The operating conditions were 15 kV accelerating voltage and a beam current of 20 nA. The beam diameter ranged from 2 to 5 μm . Relatively short counting times of 20 s on peak and 5 s on background, suitable for determining concentrations of major elements, were used. Matrix corrections were performed by the ZAF procedures [65].

The trace elements composition of apatite was analyzed using a Laser Ablation Inductively Coupled Plasma Mass Spectrometry (LA-ICP-MS). The analysis was performed at the Ore Deposit and Exploration Centre (ODEC), School of Resources and Environmental Engineering, Hefei University of Technology, Hefei, China, using a laser ablation system (Photon Machines Analyte HE with 193-nm ArF Excimer), coupled to a quadrupole-based inductively coupled plasma-mass spectrometer (ICP-MS, Agilent 7900). Ablation was done in an atmosphere of UHP He (0.9 L/min) mixed with Ar (0.87 L/min). Trace element analysis was performed using a uniform spot size diameter of 30 μm at 7 Hz with the energy of 2 J/cm² for the 40 s after measuring the gas blank for 20s. Standard reference materials NIST610, NIST612, and BCR-2G were used as external standards to plot the calibration curve [66]. Trace element compositions of silicate minerals and oxide minerals were calibrated against multiple external standardizations without applying internal standardization [67], following the procedures described in [66]. The preferred values of element concentrations for the USGS reference glasses are from the GeoReM database (<http://georem.mpch-mainz.gwdg.de>, accessed on 15 December 2022). The off-line data processing was performed using a program called ICPMSDataCal [67].

4. Results

4.1. Major Elements of Apatite

The major elements of apatite from the Fushan and Kuangshan complexes are listed in Supplementary Table S1. There are no obvious differences for CaO (52.31–56.57 wt%) and P₂O₅ (39.11–42.25 wt%) abundances among apatite grains from the Fushan and Kuangshan diorite complexes. The Cl contents of the Fushan and Kuangshan complexes range from 0.20 to 2.31 wt% (avg. 0.72 wt%) and 0.04 to 1.64 wt% (avg. 0.57 wt%), respectively. The SO₃ of the Fushan and Kuangshan complexes is in the range of 0.02–0.70 wt% (avg. 0.20 wt%) and 0–0.57 wt% (avg. 0.24 wt%), respectively. In sum, the SO₃ content of the Kuangshan complex

is higher than that of the Fushan complex, while the Cl content is higher in the Fushan complex than the Kuangshan complex. The HAp (hydroxyapatite)-FAp (fluorapatite)-CAp (chlorapatite) diagram shows that the apatite in the Fushan and Kuangshan complexes is mainly fluorapatite, which shows a banded distribution (Figure 6a), indicating that the volatile content in the melt changes rapidly, which may be influenced by the external surrounding rock, such as carbonate rock or the gypsum rock layer. The relative content of F and the ratio of $f(\text{HCl})/f(\text{H}_2\text{O})$ of apatite in each lithology showed an increasing trend, indicating that the melt in which the apatite was formed showed an evolving trend towards a high content of F or a high volatile content, and a weak higher relative content of Cl and lower content of OH. Additionally, it shows that the melt of the Fushan and Kuangshan complexes has the tendency to evolve to higher volatile contents. The SiO_2 -MnO diagram of apatite shows that the apatite in the Fushan and Kuangshan diorite complexes is magmatic in origin (Figure 6b). Diagrams are drawn using CorelKit geoscience mapping software [68].

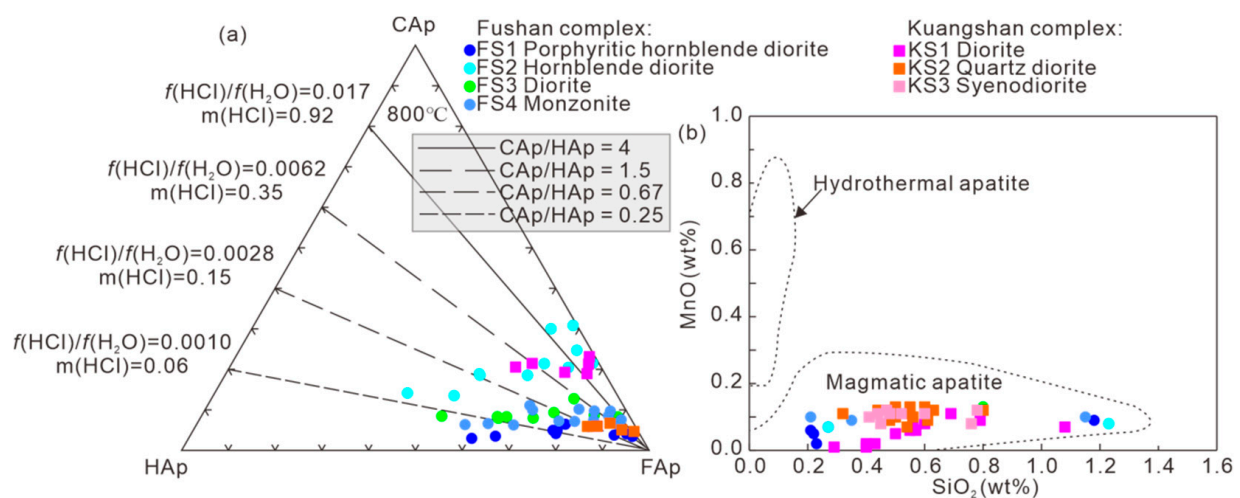


Figure 6. (a) Plot of composition of the halogen site in apatite with lines of constant Cl/OH (molar) in apatite (revised from [69,70]). (b) SiO_2 -MnO discriminant diagram of apatite type (revised from [71]). Abbreviations: FS = Fushan complex, KS = Kuangshan complex.

4.2. Trace Elements of Apatite

The trace elements of apatite composition from the investigated samples are listed in Supplementary Table S2. The Sr content of the Fushan complex is higher than that of the Kuangshan complex, while the Y content of the Fushan complex is lower than that of the Kuangshan complex (Figure 7a,b). The Sr content of the Fushan and Kuangshan complex ranges from 309.40 ppm to 1165.11 ppm (avg. 802.08 ppm) and 139.88 ppm to 1449.94 ppm (avg. 736.55 ppm), respectively. The Y content of the Fushan and Kuangshan complexes ranges from 101.27 ppm to 425.76 ppm (avg. 195.30 ppm) and 160.85 ppm to 851.56 ppm (avg. 372.59 ppm), respectively. It has Sr/Y ratios of 1.3 to 7.62 (avg. 4.34) and 0.35 to 7.63 (avg. 2.39), respectively. The content of Mn in the Fushan complex is higher than that in the Kuangshan complex (Figure 7c). The Mn varies in the Fushan and Kuangshan complexes from 156.57 to 1449.24 ppm (avg. 782.60 ppm) and 73.28 to 1073.24 ppm (avg. 703.69 ppm), respectively. The LREE content of apatite in the Kuangshan complex is similar to that of the Fushan complex, but the HREE content of the apatite is obviously higher than that of the Fushan complex in these samples (Figure 7d). The HREE content of the Fushan complex ranges from 81.95 to 382.25 ppm (avg. 152.98 ppm). The HREE content of the Kuangshan complex ranges from 137.20 to 628.01 ppm (avg. 282.07 ppm). The contents of Sr, Y, Mn, and HREE in apatite in the Kuangshan complex show positive correlation with the increase of SiO_2 in the whole rock (Figure 7). Apatite from the Fushan and Kuangshan complexes are characterized by right-inclined REE distribution patterns. Apatite from the Kuangshan complex has stronger negative Eu anomalies ($\delta\text{Eu} = 0.08\text{--}0.95$, avg = 0.64 ppm) than those

from the Fushan complex ($\delta\text{Eu} = 0.56\text{--}1.04$, avg = 0.77 ppm) (Figure 8). This indicates that plagioclase crystallization in the Fushan diorite complex occurred during or after apatite crystallization, while in the Kuangshan diorite complex, plagioclase fractionation occurred before.

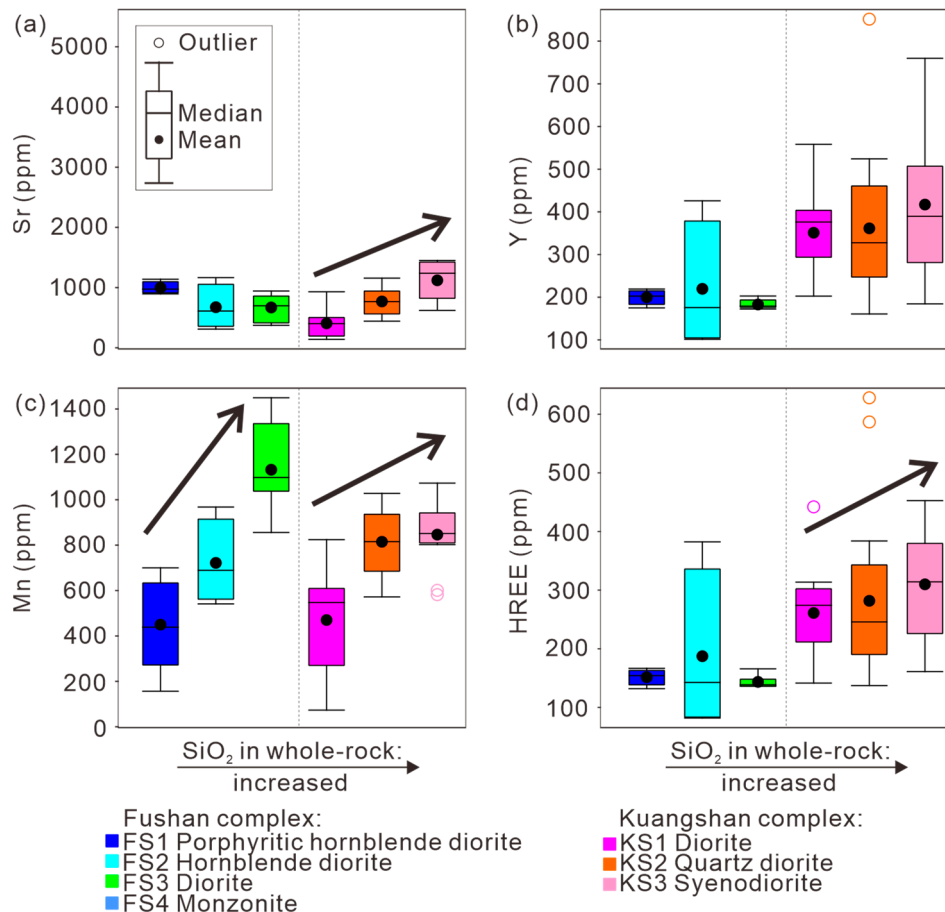


Figure 7. Trace element concentrations in apatite from the Fushan and Kuangshan complexes samples are shown as box and whisker plots. (a) Apatite Sr box plot; (b) Apatite Y box plot; (c) Apatite Mn box plot; (d) Apatite HREE box plot.

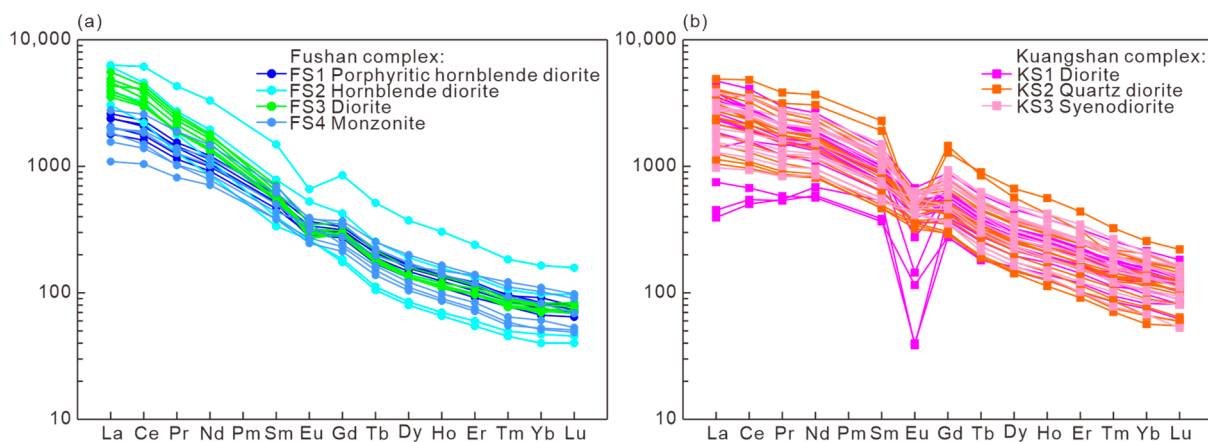


Figure 8. Chondrite-normalized REE distribution patterns of apatite. (a) Apatite from the Fushan complex; (b) Apatite from the Kuangshan complex. The chondrite REE values are from [72].

5. Discussion

5.1. Magmatic Evolution Recorded by Apatite

It is generally believed that magma in the Han–Xing region is influenced by mantle and crustal sources. Deep mantle-derived magma rises to a certain depth of the lower crust through a deep fault system and crust material is added to the magmatic system [58,62,73], then undergoes ascent, evolution, and other processes, which leave traces in rocks or minerals. The REE characteristics of the whole rock can also record these geological processes. Previous studies have shown that the magma in this region is mainly crustal contamination or source contamination, and the partition pattern of REE in the Fushan and Kuangshan complexes does not show an obvious Eu anomaly [40,58,62]. Therefore, it is speculated that large-scale crystal fractionation of plagioclase did not occur in the deep part of the lower crust.

Different from the Eu characteristics of the whole rock, the rare earth elements of apatite from both complexes show different magnitudes of negative Eu anomalies (Figure 8). The negative Eu anomaly of the Kuangshan complex (diorite, monzonite) is strong, while the negative Eu anomaly of the Fushan complex (diorite, hornblende diorite) is slight. Negative Eu anomalies in apatite are usually associated with plagioclase crystallization. However, the previous analysis obtained the information that the plagioclase crystallization of the magmatic source of the Kuangshan and Fushan complexes in the lower crust has been inhibited. Therefore, plagioclase crystallization may occur in the shallow crust, and the Kuangshan complex may have a higher proportion of plagioclase crystallization than the Fushan complex.

Extensive hydrous magmas in the lower crust are dominated by hornblende (\pm garnet) fractionation assemblage, while plagioclase crystallization is inhibited, resulting in it not showing strong negative Eu anomalies [74]. The REE characteristics of whole rock and apatite in the Fushan and Kuangshan complexes are consistent with the suppression of plagioclase crystallization in the deep crust, and the basic magma formed near the lower crust has high water content. Deep plagioclase crystallization inhibited by aqueous magma rising from the lower crust will promote the accumulation and enrichment of volatiles [75,76]. Comparing the data in the study area with the fractional crystallization simulation data of hydrous magma [7] (Figure 9), it is found that the Sr/Y vs. Eu/Eu* diagram of apatite is more sensitive to the magmatic evolution process exhibited by apatite. The comparison of Sr/Y vs. Eu/Eu* diagrams shows that the Fushan complex is similar to the Kuangshan complex, and the maximum values of Sr/Y and Eu/Eu* are located in the initial melt (amp 66%, cpx 34%; mid- to lower-crust, 1.0 GPa and 4.5 wt% H₂O; [77]), in the vicinity of 60%. Both experienced the evolution of amphibole separation in the deep part and formed a similar magma melt that rose to the shallow part of the crust and then crystallized. During the crystallization process of magma in the shallow part of the crust, the Kuangshan complex (5%–60%) maintained a higher crystallization ratio than the Fushan complex (5%–20%). That is, the Kuangshan complex has more plagioclase than the Fushan complex, resulting in more volatile accumulation and enrichment in the Kuangshan complex. Therefore, the evolution process of the Kuangshan complex source magma is more conducive to mineralization.

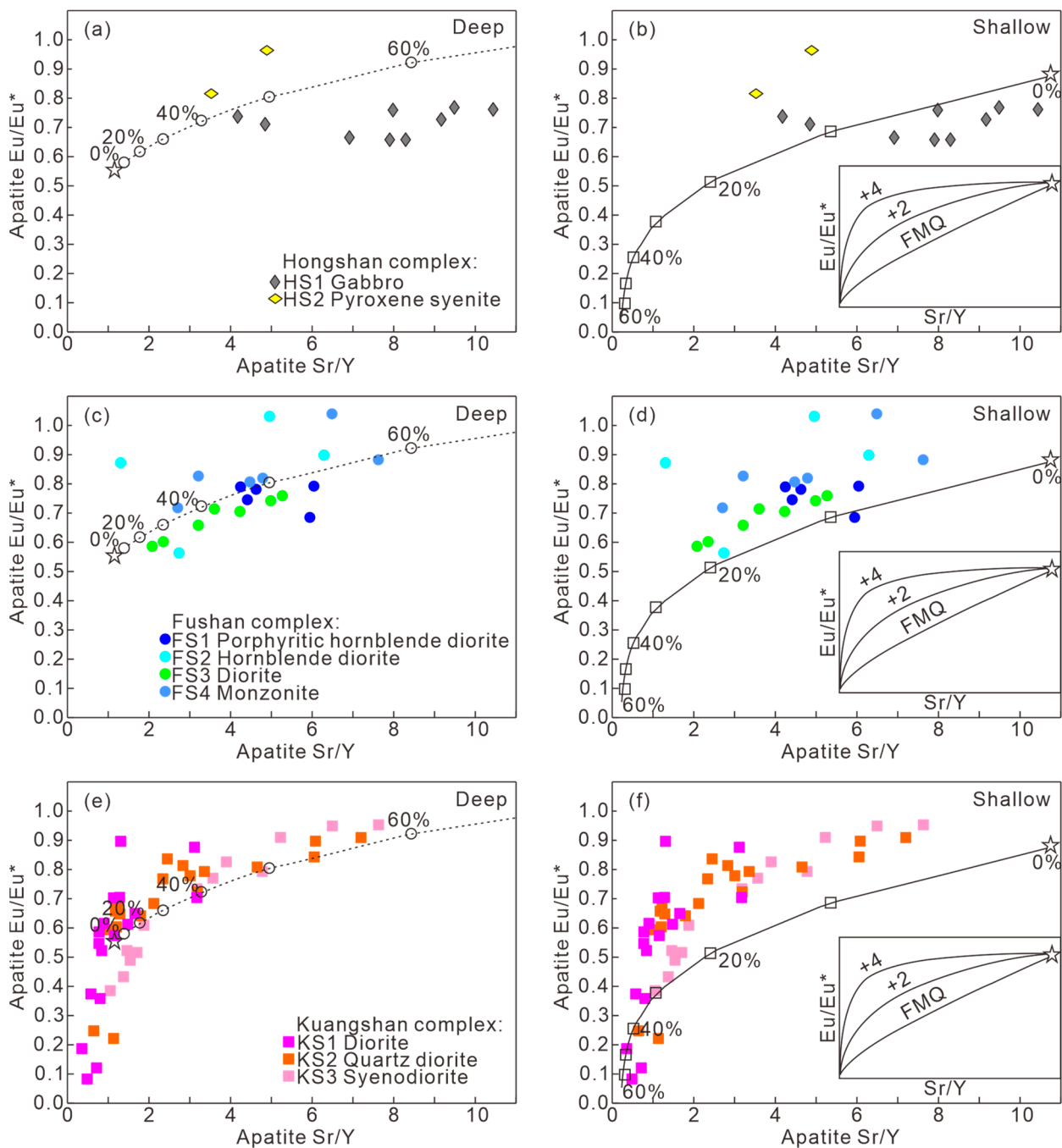


Figure 9. Diagrams of Sr/Y-Eu/Eu* in apatite. The deep fractional crystallization model (amp (66%) cpx (34%)) for the Hongshan (a), Fushan (c), and Kuangshan (e) complexes, the shallow fractional crystallization model (amp (23%) pl (77%)) for the Hongshan (b), Fushan (d), and Kuangshan (f) complexes. The data of the Hongshan complex is quoted from [78–80]. The start of each fractionation path and percentage of crystallization is from [7].

5.2. Indication of Oxygen Fugacity of Apatite

The contents of variable valence elements such as Eu, Ce, Mn, and S in apatite are easily affected by the change of redox conditions in melt and are often used to indicate the change of oxygen fugacity. The apatite oxygen fugacity meter is often used to compare the oxygen fugacity of magma in the study of genetic mineralogy, and is further recommended as an indicator for mineral exploration [2,17–26]. In the ore deposit genesis study, apatite oxygen fugacity meters are mostly used in copper-molybdenum deposits, but rarely in skarn iron

deposits. Since Eu is not only affected by oxygen fugacity, plagioclase crystallization will also affect it [81]. However, the feldspar crystallization ratios in the complexes in this study area are quite different, which will have a great impact on the apatite Eu oxygen fugacity meter. The key of the Ce oxygen fugacity meter is Ce^{4+} . Given the extremely weak content of Ce^{4+} in the apatite system, its reliability is questionable [81–83]. The apatite SO_3 content can also indicate the redox state of magma sources or related fluids [5,84]. The apatite SO_3 content in the Fushan complex ranges from 0.02 to 0.42, with an average of 0.20. The apatite SO_3 content of the Kuangshan complex ranges from 0.02 to 0.57, with an average value of 0.24 (Figure 10a). The Kuangshan complex has a higher apatite SO_3 content. Although questions regarding the reliability of the apatite Mn oxygen fugacity meter have been raised, it may still be effective when applied in intermediate-acidic magmatic systems [21]. The oxygen fugacity by apatite calculated in the Fushan complex is $\Delta FMQ - 2.1 \sim \Delta FMQ + 7.22$, with an average value of $\Delta FMQ + 2.54$. The oxygen fugacity by apatite calculated in the Kuangshan complex is $\Delta FMQ + 1.04 \sim \Delta FMQ + 7.27$, with an average value of $\Delta FMQ + 4.77$ (Figure 10b). The Kuangshan complex has a higher oxygen fugacity than the apatite of the Fushan complex. Through comparison of the oxygen fugacity box diagram, it is found that the overall oxygen fugacity of the Kuangshan complex in the melt is high and there is a low oxygen fugacity outlier. These characteristics of oxygen fugacity may reflect the change process from low oxygen fugacity to high oxygen fugacity of ore-bearing hydrothermal fluid. A wide oxygen fugacity range reflects the existence of a multistage magma chamber during magma ascent, especially in shallow limestones and evaporites, which leads to the rapid rise of oxygen fugacity and even the occurrence of an outlier. These characteristics indicate that high oxygen fugacity or an oxygen fugacity outlier is favorable for mineralization.

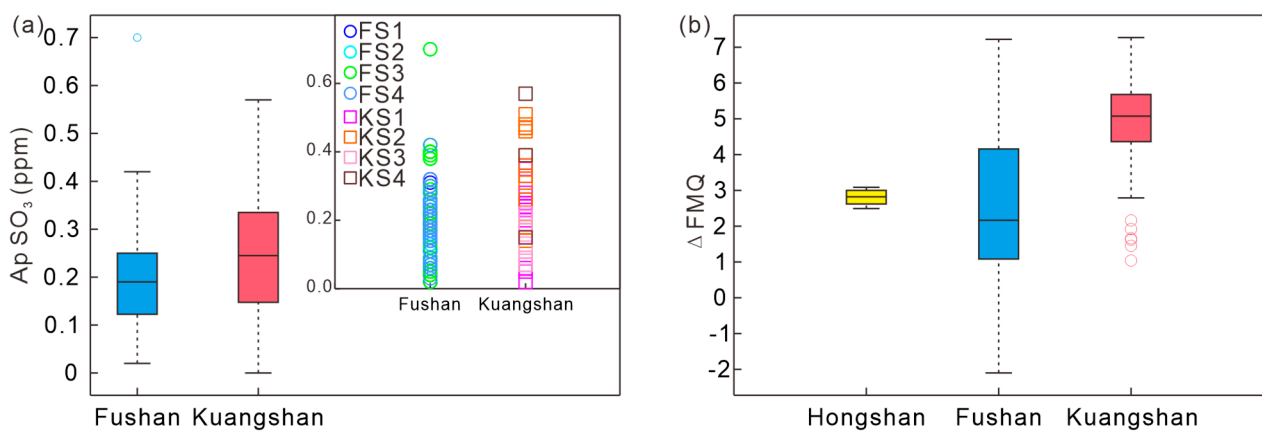


Figure 10. (a) Diagrams of SO_3 content in apatite (Fushan complex: FS1—Porphyritic hornblende diorite, FS2—Hornblende diorite, FS3—Diorite, FS4—Monzonite; Kuangshan complex: KS1—Diorite, KS2—Quartz diorite, KS3—Syenodiorite, KS4—Quartz monzonite); (b) Diagrams of ΔFMQ in the Hongshan, Fushan and Kuangshan complexes. The data of the Hongshan complex is quoted from [78–80].

In view of the comprehensive comparison of various oxygen fugacity characteristics, we believe that the Kuangshan complex has relatively higher oxygen fugacity characteristics, which may be more conducive to the formation of a larger-scale magnetite deposit.

5.3. Evolution Process of Magmatic Volatiles Reflected by Apatite

The evolution of magma volatiles plays an important role in controlling mineralization [8–16]. Chlorine, fluorine, and sulfur in ore-forming fluids are particularly critical and can form ligands with ore-forming elements such as copper, gold, lead, zinc, iron, molybdenum, and other cations such as H^+ , K^+ , Na^+ , and Ca^{2+} . These can transport them to appropriate locations to cause alteration or mineralization [85]. Because apatite is rich

in volatile elements such as F, Cl, OH, and S, the volatile content in its equilibrium melt can be calculated. Many scholars have studied the volatile content of magma in porphyry metallogenic system by apatite, showing that magma melt after extensive fluid exsolution may form a porphyry deposit if it has high content of F, Cl, and SO_3 [9,12,14,15,86]. There are few related studies on the skarn-type mineralization system. Zhou et al. (2022) studied skarn deposits in Daye, eastern China, and found that silicate melts with high volatile components (F, Cl, SO_3 , etc.) are also conducive to mineralization, copper is moderately correlated with volatile components in silicate melts, while iron ore is correlated with higher volatile components (F, Cl, SO_3 , etc.) [8].

Based on the thermodynamic distribution model of apatite/melt F and Cl [4] and the calculation formula of apatite melt S content [3,5], the contents of Cl, F, and SO_3 in the Fushan and Kuangshan complexes were calculated in this study (Figure 11). The content of F, Cl, and SO_3 in the Fushan complex magma ranges from 1042 to 5201 ppm (average 2488 ppm), from 500 to 14,400 ppm (average 3400 ppm), and from 20 to 1660 ppm (average 90 ppm), respectively. The magma of the Kuangshan complex contains 1550–3709 ppm F (average 2632 ppm), 1000–10,100 ppm Cl (average 4100 ppm), and 20–720 ppm SO_3 (average 140 ppm). The average values of F, Cl, and SO_3 in the two complexes increase sequentially from the weak ore-forming Fushan complex to the strong ore-forming Kuangshan complex. Although when distinguishing between strong and weak ore-forming complexes, the Kuangshan complex has only slightly higher average values of F, Cl, and SO_3 than the Fushan complex, which also shows that high fluorine, high chlorine, and high SO_3 in the complex are beneficially ore forming. In addition, the Fushan complex has a larger range of data variation, which may be related to the fractional crystallization of the multistage magma chambers formed during the ascent of its magma.

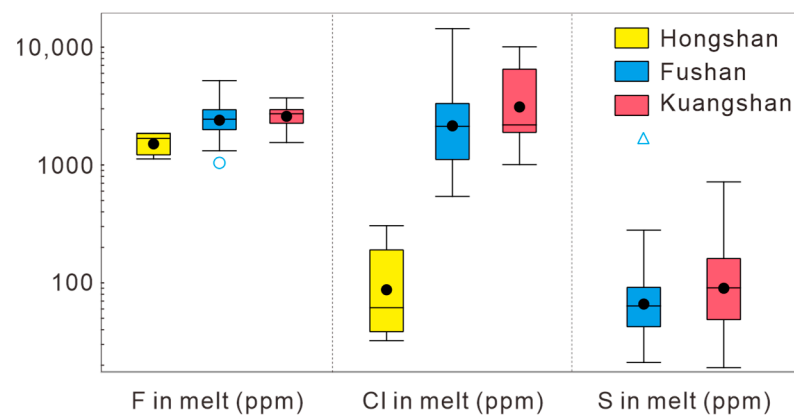


Figure 11. Boxplots of F, Cl, and S in melt (○—mild outlier; △—extreme outlier). The data of the Hongshan complex is quoted from [78–80].

5.4. Contrast of the Iron-Bearing Complex and the Barren Complex

This study evaluates the ore-forming potential of the complex by studying the magmatic evolution process and melt-fluid oxygen fugacity and volatiles of the complex so as to serve as a reference index in the early stage of mineral exploration. Because the two complexes are skarn iron ore host complexes with different ore-forming scales, their apatite analysis data overlap more, and the difference is relatively small. Although the small difference of one index is not high confidence, the confidence of multiple index differences will be enough to reveal the favorable ore-forming factors when they constitute the combination difference of similar gene profiles. Compared with the Fushan complex, the Kuangshan complex has a higher magmatic evolution degree, higher oxygen fugacity, and higher F-Cl-S volatile content, which is the difference of metallogenic gene combination, which can indicate the metallogenic potential when the complex has the characteristics of high evolution degree, oxygen fugacity, and high F-Cl-S volatile content. In order to verify

the distinction between an iron-bearing complex and a barren complex, a barren complex needs to be introduced for verification and comparison.

Introducing barren skarn-type iron ore complexes outside the region for comparison will bring about huge differences between the comparison objects, such as the regional tectonic background, sedimentary surrounding rocks, magma source areas, and intrusion features. This makes it difficult to distinguish which variables lead to the difference in mineralization. In order to minimize the impact of too many variable differences on the verification, the only barren complex (Hongshan complex) in the Han–Xing area was selected for comparison. Although the Hongshan complex is mainly composed of syenite, and the surrounding sedimentary rocks are non-carbonate rocks, there are also problems such as large differences in the composition of host rocks and sedimentary surrounding rocks; however, from the perspective of preliminary screening of iron-rich complexes in regional mineral exploration, these effects can be ignored. Hence, in order to better prove the validity of the differences in apatite mineralization gene combinations, the barren Hongshan complex in the region was added to the comparison.

The Hongshan complex has similar unobvious whole-rock Eu anomalies to the Fushan and Kuangshan complexes, and the in situ trace elements of apatite show obvious Eu negative anomalies to varying degrees [58]. The Kuangshan complex is similar, and the deep evolution of magma is dominated by hornblende crystallization. The magma of the Hongshan complex (65%) (Figure 9a) is more basic than that of the Fushan and Kuangshan complex (60%) (Figure 9c,e) when it rises to the middle and shallow crust. The crystallization rate of plagioclase in the shallow crust is lower (Figure 9b,d,f; the Hongshan complex 0%–15%; the Fushan complex 5%–20%; the Kuangshan complex 5%–60%), the accumulated volatiles are fewer, and the magmatic evolution degree is lower than that of the Fushan and Kuangshan complexes. The Hongshan complex has lower oxygen fugacity (Figure 10b) and F-Cl volatiles (Figure 11) than the Fushan complex and Kuangshan complex. After the final comparison, it was found that the Hongshan complex has the characteristics of low magmatic evolution, low oxygen fugacity, and low F-Cl; therefore, its metallogenic potential is poor. Hence, the differences in apatite mineralization gene combinations are basically consistent in the complexes in the Han–Xing area.

The oxygen fugacity characteristics need to be emphasized here. Oxygen fugacity is usually closely related to changes in the external environment. The variation range of oxygen fugacity is related to the multistage magma chamber formed by magma in the middle and shallow crust and is also affected by the near-surface strata (carbonate rocks or gypsum rocks). The crystallization depth can be calculated by hornblende. The magma chamber of the Hongshan complex is 3–9 km deep and divided into two stages [79]. The sedimentary surrounding rock is sandstone, mudstone, shale, etc., resulting in a small and low variation range of oxygen fugacity. The crystal depth of the magma chamber of the Fushan complex is 1–26 km, and the magma chamber is almost continuously distributed ([87]; Liang, unpublished). The sedimentary surrounding rock is a carbonate rock, resulting in the largest and high variation range of oxygen fugacity. The crystallization depth of magma chamber of the Kuangshan complex is 1–21 km, and the magma chamber is divided into three stages, of which, the first to second stages (1–8 km) are dominant (Liang, unpublished). The sedimentary surrounding rock is a carbonate rock, resulting in a large and high variation range of oxygen fugacity (mild outliers).

It can be seen that there are many factors affecting the metallogenic potential of a complex. When evaluating the metallogenic potential, it is necessary to build a metallogenic gene combination characteristic model composed of the magmatic evolution process, oxygen fugacity, volatile components, carbonate rock, ore structure, etc., and then distinguish the systematic differences of the complex to draw a conclusion on the metallogenic possibility.

5.5. Preliminary Study on Favorable Ore-Forming Lithology of Skarn Iron Deposit Boarding Complex

A large number of studies have shown that magmatite related to skarn copper deposits have obvious metallogenic specificity [39], which are generally related to diorites. The magmatite related to skarn iron deposits do not show specific properties, but are distributed from basic rock, intermediate rock, intermediate-acid rock, and acid rock. For example, the surrounding rocks of the Cihai iron ore deposit in Xinjiang, China are diabase [41]; the surrounding rocks of the Tieshan ore deposit in Daye, China are quartz-bearing diorite, biotite diopside diorite, syenite diorite, and porphyritic quartz-bearing diorite [42]; the surrounding rocks of the Sangan iron deposit in Iran are syenite-granite and quartz monzonite [45]; and the surrounding rocks of the Makeng iron deposit in Fujian, China are granite [43]. The characteristics of the skarn iron deposit in Han–Xing region are more significant. The lithology of the surrounding rocks near the skarn-type iron ore bodies in the Han–Xing area is diverse. A variety of lithologies, such as diorite, monzodiorite, and porphyritic hornblende monzonite, have been found around the Fushan iron deposit, and the intrusion relationship of each lithology is very complicated [44]. In the Kuangshan complex, the surrounding rock of the Xishimen iron deposit contains diorite, syenite diorite, hornblende monzonite, monzonite, diorite porphyrite, etc. [40]. Hence, the lithology of the two complexes has no specificity of mineralization.

The oxygen fugacity and volatile content of each lithology of the two complexes calculated by apatite do not show obvious correlation with their respective lithologies, which indicates that the ore-forming lithology of iron ore may not be the main factor. In order to study the genesis of skarn-type iron ore or to explore iron ore, it is necessary to comprehensively consider other factors, such as the structure and lithology of the surrounding rock.

Although there are many kinds of lithology in the complex in the Han–Xing area, and it is not one lithology, it is still effective to study the prospecting potential of the complicated complex as a whole.

6. Conclusions

(1) Our apatite geochemical data indicate that the Fushan and Kuangshan complexes were primarily formed through amphibole fractional crystallization during deep processes, whereas the magma for the Kuangshan complex experienced extensive plagioclase fractional crystallization during shallow processes, which is more favorable for the formation of iron deposits.

(2) Based on apatite composition the Kuangshan complex show higher oxygen fugacity and volatiles such as F, Cl and S, compared with the Fushan complex. The oxygen fugacity and volatiles plutonic complexes have certain indicative significance for mineral exploration.

(3) There are a variety of intrusive rocks related to skarn iron deposit mineralization in the Han–Xing area. Each independent complex body in this area should be studied as an independent unit to study the possibility of mineralization.

Supplementary Materials: The following supporting information can be downloaded at: <https://www.mdpi.com/article/10.3390/min13040469/s1>, Table S1. EMPA results of apatite from diorite in the Fushan and Kuangshan complexes. Table S2. LA-ICP-MS results of apatite from diorite in the Fushan and Kuangshan complexes

Author Contributions: X.L.: writing-original draft preparation, data curation; F.W.: funding acquisition, writing-review and editing; J.Z. (Juquan Zhang): writing-review and editing; L.Z.: methodology, writing-review and editing; J.Z. (Junwu Zhang): software, writing-review and editing; J.W.: supervision. All authors have read and agreed to the published version of the manuscript.

Funding: This study is financially supported by the National Natural Science Foundation of China (Grant nos. 91962218, 42273065, 41873034, 41602028).

Data Availability Statement: Data presented was original and not inappropriately selected, manipulated, enhanced, or fabricated.

Acknowledgments: Two anonymous reviewers are thanked for their valuable comments and suggestions that improved this paper significantly.

Conflicts of Interest: The authors declare no conflict of interest.

References

1. Bouzari, F.; Hart, C.J.R.; Bissig, T.; Barker, S. Hydrothermal Alteration Revealed by Apatite Luminescence and Chemistry: A Potential Indicator Mineral for Exploring Covered Porphyry Copper Deposits. *Econ. Geol.* **2016**, *111*, 1397–1410. [[CrossRef](#)]
2. Mao, M.; Rukhlov, A.S.; Rowins, S.M.; Spence, J.; Coogan, L.A. Apatite trace element compositions: A robust new tool for mineral exploration*. *Econ. Geol.* **2016**, *111*, 1187–1222. [[CrossRef](#)]
3. Parat, F.; Holtz, F.; Klügel, A. S-rich apatite-hosted glass inclusions in xenoliths from La Palma: Constraints on the volatile partitioning in evolved alkaline magmas. *Contrib. Mineral. Petrol.* **2011**, *162*, 463–478. [[CrossRef](#)]
4. Li, H.; Hermann, J. Chlorine and fluorine partitioning between apatite and sediment melt at 2.5 GPa, 800 °C: A new experimentally derived thermodynamic model. *Am. Mineral.* **2017**, *102*, 580–594. [[CrossRef](#)]
5. Peng, G.; Luhr, J.F.; Mcgee, J.J. Factors controlling sulfur concentrations in volcanic apatite. *Am. Mineral.* **1997**, *82*, 1210–1224. [[CrossRef](#)]
6. Webster, J.D.; Piccoli, P.M. Magmatic Apatite: A Powerful, Yet Deceptive, Mineral. *Elements* **2015**, *11*, 177–182. [[CrossRef](#)]
7. Nathwani, C.L.; Loader, M.A.; Wilkinson, J.J.; Buret, Y.; Sievwright, R.H.; Hollings, P. Multi-stage arc magma evolution recorded by apatite in volcanic rocks. *Geology* **2020**, *48*, 323–327. [[CrossRef](#)]
8. Zhou, R.; Wen, G.; Li, J.; Jiang, S.; Hu, H.; Deng, X.; Zhao, X.; Yan, D.; Wei, K.; Cai, H.; et al. Apatite chemistry as a petrogenetic-metallogenic indicator for skarn ore-related granitoids: An example from the Daye Fe–Cu–(Au–Mo–W) district, Eastern China. *Contrib. Mineral. Petrol.* **2022**, *177*, 23. [[CrossRef](#)]
9. Huang, M.; Zhu, J.; Bi, X.; Xu, L.; Xu, Y. Low magmatic Cl contents in giant porphyry Cu deposits caused by early fluid exsolution: A case study of the Yulong belt and implication for exploration. *Ore Geol. Rev.* **2022**, *141*, 104664. [[CrossRef](#)]
10. Duan, D.; Jiang, S. Using apatite to discriminate synchronous ore-associated and barren granitoid rocks: A case study from the Edong metallogenic district, South China. *Lithos* **2018**, *310–311*, 369–380. [[CrossRef](#)]
11. Duan, D.; Jiang, S.; Tang, Y.; Wu, Y.; Zhou, B.; Zhu, J. Chlorine and sulfur evolution in magmatic rocks: A record from amphibole and apatite in the Tonglvshan Cu-Fe (Au) skarn deposit in Hubei Province, south China. *Ore Geol. Rev.* **2021**, *137*, 104312. [[CrossRef](#)]
12. Li, Q.; Sun, X.; Lu, Y.; Wang, F.; Hao, J. Apatite and zircon compositions for Miocene mineralizing and barren intrusions in the Gangdese porphyry copper belt of southern Tibet: Implication for ore control. *Ore Geol. Rev.* **2021**, *139*, 104474. [[CrossRef](#)]
13. Wang, D.; Zhu, J.; Bi, X.; Fu, S.; Lu, Z.; Wu, L.; Hu, R. Increasing sulfur and chlorine contents in ore-forming magmas: The key to Pulang porphyry Cu-Au formation, SW China. *Ore Geol. Rev.* **2021**, *139*, 104518. [[CrossRef](#)]
14. Xu, B.; Hou, Z.; Griffin, W.L.; Lu, Y.; Belousova, E.; Xu, J.; O'Reilly, S.Y. Recycled volatiles determine fertility of porphyry deposits in collisional settings. *Am. Mineral.* **2021**, *106*, 656–661. [[CrossRef](#)]
15. Zhu, J.; Richards, J.P.; Rees, C.; Creaser, R.; Dufrane, S.A.; Locock, A.; Petrus, J.A.; Lang, J. Elevated Magmatic Sulfur and Chlorine Contents in Ore-Forming Magmas at the Red Chris Porphyry Cu-Au Deposit, Northern British Columbia, Canada. *Econ. Geol.* **2018**, *113*, 1047–1075. [[CrossRef](#)]
16. Parra-Avila, L.A.; Hammerli, J.; Kemp, A.I.S.; Rohrlach, B.; Loucks, R.; Lu, Y.; Williams, I.S.; Martin, L.; Roberts, M.P.; Fiorentini, M.L. The long-lived fertility signature of Cu–Au porphyry systems: Insights from apatite and zircon at Tampakan, Philippines. *Contrib. Mineral. Petrol.* **2022**, *177*, 18. [[CrossRef](#)]
17. Zhang, L.; Chen, Z.; Wang, F.; Zhou, T. Apatite geochemistry as an indicator of petrogenesis and uranium fertility of granites: A case study from the Zhuguangshan batholith, South China. *Ore Geol. Rev.* **2021**, *128*, 103886. [[CrossRef](#)]
18. Cao, M.; Li, G.; Qin, K.; Seitmuratova, E.Y.; Liu, Y. Major and Trace Element Characteristics of Apatites in Granitoids from Central Kazakhstan: Implications for Petrogenesis and Mineralization. *Resour. Geol.* **2012**, *62*, 63–83. [[CrossRef](#)]
19. Imai, A.; Listanco, E.L.; Fujii, T. Petrologic and sulfur isotopic significance of highly oxidized and sulfur-rich magma of Mt. Pinatubo, Philippines. *Geology* **1993**, *21*, 699–702. [[CrossRef](#)]
20. Liu, M.; Zhou, M.; Su, S.; Chen, X. Contrasting Geochemistry of Apatite from Peridotites and Sulfide Ores of the Jinchuan Ni-Cu Sulfide Deposit, NW China. *Econ. Geol.* **2021**, *116*, 1073–1092. [[CrossRef](#)]
21. Miles, A.J.; Graham, C.M.; Hawkesworth, C.J.; Gillespie, M.R.; Hinton, R.W.; Bromiley, G.D. Apatite: A new redox proxy for silicic magmas? *Geochim. Cosmochim. Acta* **2014**, *132*, 101–119. [[CrossRef](#)]
22. Pan, L.; Hu, R.; Wang, X.; Bi, X.; Zhu, J.; Li, C. Apatite trace element and halogen compositions as petrogenetic-metallogenic indicators: Examples from four granite plutons in the Sanjiang region, SW China. *Lithos* **2016**, *254–255*, 118–130. [[CrossRef](#)]
23. Parat, F.; Holtz, F. Sulfur partitioning between apatite and melt and effect of sulfur on apatite solubility at oxidizing conditions. *Contrib. Mineral. Petrol.* **2004**, *147*, 201–212. [[CrossRef](#)]
24. Qi, H.; Yang, X.; Lu, S.; Lee, I.; Kim, Y. Petrogenetic and metallogenic implications of the Late Mesozoic intrusive rocks in the Xuancheng ore district, eastern China: Insight from in situ analysis of apatite. *Geosci. J.* **2022**, *26*, 113–128. [[CrossRef](#)]

25. Xing, K.; Shu, Q.; Lentz, D.R.; Wang, F. Zircon and apatite geochemical constraints on the formation of the Huojihe porphyry Mo deposit in the Lesser Xing'an Range, NE China. *Am. Mineral.* **2020**, *105*, 382–396. [[CrossRef](#)]
26. Zhang, S.; Yang, L.; He, W.; Gao, X.; Liu, X. Melt volatile budgets and magma evolution revealed by diverse apatite halogen and trace elements compositions: A case study at Pulang porphyry Cu-Au deposit, China. *Ore Geol. Rev.* **2021**, *139*, 104509. [[CrossRef](#)]
27. Cao, K.; Yang, Z.; Hou, Z.; White, N.C.; Yu, C. Contrasting porphyry Cu fertilities in the Yidun arc, eastern Tibet: Insights from zircon and apatite compositions and implications for exploration. *Seg. Spec. Publ.* **2021**, *24*, 231–255.
28. Wang, R.; Luo, C.; Xia, W.; He, W.; Liu, B.; Huang, M.; Hou, Z.; Zhu, D. Role of alkaline magmatism in formation of porphyry deposits in nonarc settings: Gangdese and Sanjiang metallogenic belts. *Seg. Spec. Publ.* **2021**, *24*, 205–229.
29. Cao, K.; Yang, Z.; White, N.C.; Hou, Z. Generation of the Giant Porphyry Cu-Au Deposit by Repeated Recharge of Mafic Magmas at Pulang in Eastern Tibet. *Econ. Geol.* **2022**, *117*, 57–90. [[CrossRef](#)]
30. Shen, J.; Santosh, M.; Li, S.; Zhang, H.; Yin, N.; Dong, G.; Wang, Y.; Ma, G.; Yu, H. The Beiminghe skarn iron deposit, eastern China: Geochronology, isotope geochemistry and implications for the destruction of the North China Craton. *Lithos* **2013**, *156–159*, 218–229. [[CrossRef](#)]
31. Deng, X.; Li, J.; Wen, G. U-Pb Geochronology of Hydrothermal Zircons from the Early Cretaceous Iron Skarn Deposits in the Handan-Xingtai District, North China Craton. *Econ. Geol.* **2015**, *110*, 2159–2180. [[CrossRef](#)]
32. Sun, Y.; Xiao, L.; Zhan, Q.; Wu, J.; Zhu, D.; Huang, W.; Bai, M.; Zhang, Y. Petrogenesis of the Kuangshancun and Hongshan intrusive complexes from the Handan–Xingtai district: Implications for iron mineralization associated with Mesozoic magmatism in the North China Craton. *J. Asian Earth Sci.* **2015**, *113*, 1162–1178. [[CrossRef](#)]
33. Jin, Z.; Zhang, Z.; Hou, T.; Santosh, M.; Han, L. Genetic relationship of high-Mg dioritic pluton to iron mineralization: A case study from the Jinling skarn-type iron deposit in the North China Craton. *J. Asian Earth Sci.* **2015**, *113*, 957–979. [[CrossRef](#)]
34. Zhang, J.; Li, S.; Santosh, M.; Wang, J.; Li, Q. Mineral chemistry of high-Mg diorites and skarn in the Han–Xing Iron deposits of South Taihang Mountains, China: Constraints on mineralization process. *Ore Geol. Rev.* **2015**, *64*, 200–214. [[CrossRef](#)]
35. Sun, Y.; Wu, T.; Xiao, L.; Bai, M.; Zhang, Y. U-Pb ages, Hf-O isotopes and trace elements of zircons from the ore-bearing and ore-barren adakitic rocks in the Handan-Xingtai district: Implications for petrogenesis and iron mineralization. *Ore Geol. Rev.* **2019**, *104*, 14–25. [[CrossRef](#)]
36. Sun, Y.; Wu, T.; Xiao, L.; Bai, M.; Zhang, Y. Contrasting mineralogical-geochemical compositions of ore-bearing and ore-barren intrusive complexes in the Handan-Xingtai district, North China Craton: Implications for the iron mineralization. *Lithos* **2019**, *350–351*, 105244. [[CrossRef](#)]
37. Zhang, J.; Yan, L.; Santosh, M.; Li, S.; Lu, J.; Wang, D.; Liang, X.; Wang, L.; Li, Y. Tracing the genesis of skarn-type iron deposit in central North China Craton: Insights from mineral zoning textures in ore-forming intrusion. *Geol. J.* **2020**, *55*, 6280–6295. [[CrossRef](#)]
38. Wen, G.; Li, J.; Hofstra, A.H.; Koenig, A.E.; Cui, B. Textures and compositions of clinopyroxene in an Fe skarn with implications for ore-fluid evolution and mineral-fluid REE partitioning. *Geochim. Cosmochim. Acta* **2020**, *290*, 104–123. [[CrossRef](#)]
39. Meinert, L.D.; Dipple, G.M.; Nicolescu, S. World skarn deposits. In *One Hundredth Anniversary Volume*; Hedenquist, J.W., Thompson, J.F.H., Goldfarb, R.J., Richards, J.P., Eds.; Society of Economic Geologists: Littleton, CO, USA, 2005.
40. Wei, H. Geological Characteristics and Genesis of Xishimen Skarn Iron Deposit in Handan. Master's Thesis, Shijiazhuang University of Economics, Shijiazhuang, China, 2011. (In Chinese with English abstract)
41. Qi, T. The Large-Scale Metallogenic Process of Iron in the Cihai Giant Iron District, Xinjiang Province. Master's Thesis, China University of Geosciences, Beijing, China, 2013. (In Chinese with English abstract)
42. Hu, H. Mineralogical, Geochemical, and Geochronological Constrains on the Genesis of Iron Deposits in the Daye District, Eastern China. Ph.D. Thesis, China University of Geosciences, Wuhan, China, 2014. (In Chinese with English abstract).
43. Zhang, Z.; Zhang, C. Skarn mineral characteristics and zonation of the Makeng Fe-Mo deposit in Fujian Province. *Acta Petrol. Sin.* **2014**, *30*, 1339–1354, (In Chinese with English abstract)
44. Meng, W. Characteristics and Origin of Magnetite in Fushan Iron Deposit, Shexian Country, Hebei Province. Master's Thesis, China University of Geosciences, Beijing, China, 2020. (In Chinese with English abstract)
45. Mehrabi, B.; Ghasemi Siani, M.; Zhang, R.; Neubauer, F.; Lentz, D.R.; Fazel, E.T.; Shahraki, B.K. Mineralogy, petrochronology, geochemistry, and fluid inclusion characteristics of the Dardvay skarn iron deposit, Sangan mining district, NE Iran. *Ore Geol. Rev.* **2021**, *134*, 104146. [[CrossRef](#)]
46. Qian, Q.; Hermann, J. Formation of High-Mg Diorites through Assimilation of Peridotite by Monzodiorite Magma at Crustal Depths. *J. Petrol.* **2010**, *51*, 1381–1416. [[CrossRef](#)]
47. Chen, B.; Jahn, B.M.; Arakawa, Y.; Zhai, M.G. Petrogenesis of the Mesozoic intrusive complexes from the southern Taihang Orogen, North China Craton: Elemental and Sr–Nd–Pb isotopic constraints. *Contrib. Mineral. Petrol.* **2004**, *148*, 489–501. [[CrossRef](#)]
48. Chen, B.; Tian, W.; Jahn, B.M.; Chen, Z.C. Zircon SHRIMP U–Pb ages and in-situ Hf isotopic analysis for the Mesozoic intrusions in South Taihang, North China craton: Evidence for hybridization between mantle-derived magmas and crustal components. *Lithos* **2008**, *102*, 118–137. [[CrossRef](#)]
49. Wang, Y.; Fan, W.; Zhang, H.; Peng, T. Early Cretaceous gabbroic rocks from the Taihang Mountains: Implications for a paleosubduction-related lithospheric mantle beneath the central North China Craton. *Lithos* **2006**, *86*, 281–302. [[CrossRef](#)]

50. Xu, W.; Yang, D.; Gao, S.; Pei, F.; Yu, Y. Geochemistry of peridotite xenoliths in Early Cretaceous high-Mg# diorites from the Central Orogenic Block of the North China Craton: The nature of Mesozoic lithospheric mantle and constraints on lithospheric thinning. *Chem. Geol.* **2010**, *270*, 257–273. [[CrossRef](#)]
51. Huo, Y.; Su, S.; Yang, Y.; Gu, D. The evidence for lithospheric thinning of Mesozoic North China Craton: Taking Guzhen intrusion complex as an example. *Acta Petrol. Sin.* **2019**, *35*, 989–1014. (In Chinese with English abstract)
52. Wu, F.; Yang, J.; Xu, Y.; Wilde, S.A.; Walker, R.J. Destruction of the North China Craton in the Mesozoic. *Annu. Rev. Earth Planet. Sci.* **2019**, *47*, 173–195. [[CrossRef](#)]
53. Li, S.; Santosh, M.; Zhang, H.; Shen, J.; Dong, G.; Wang, J.; Zhang, J. Inhomogeneous lithospheric thinning in the central North China Craton: Zircon U–Pb and S–He–Ar isotopic record from magmatism and metallogeny in the Taihang Mountains. *Gondwana Res.* **2013**, *23*, 141–160. [[CrossRef](#)]
54. Zhu, R.; Yang, J.; Wu, F. Timing of destruction of the North China Craton. *Lithos* **2012**, *149*, 51–60. [[CrossRef](#)]
55. Shen, J.; Li, S.; Santosh, M.; Dong, G.; Wang, Y.; Liu, H.; Peng, Z.; Zhang, Z. Zircon U–Pb geochronology of the basement rocks and dioritic intrusion associated with the Fushan skarn iron deposit, southern Taihang Mountains, China. *J. Asian Earth Sci.* **2015**, *113*, 1132–1142. [[CrossRef](#)]
56. Li, S.; Santosh, M. Metallogeny and craton destruction: Records from the North China Craton. *Ore Geol. Rev.* **2014**, *56*, 376–414. [[CrossRef](#)]
57. Zhang, Z.; Hou, T.; Santosh, M.; Li, H.; Li, J.; Zhang, Z.; Song, X.; Wang, M. Spatio-temporal distribution and tectonic settings of the major iron deposits in China: An overview. *Ore Geol. Rev.* **2014**, *57*, 247–263. [[CrossRef](#)]
58. Li, Y. Mesozoic Magmatism Time Limit of the South Taihang and Its Tectonic Significance. Master’s Thesis, Hebei GEO University, Shijiazhuang, China, 2019. (In Chinese with English abstract)
59. Peng, T.; Wang, Y.; Fan, W.; Guo, F.; Peng, B. SHRIMP zircon U–Pb geochronology of the diorites for southern Taihang Mountains in the North China Interior and its petrogenesis. *Acta Petrol. Sin.* **2004**, *5*, 264–273. (In Chinese with English abstract)
60. Wang, Y. The Characteristics of Fushan Iron Deposit, Handan, Hebei Province, China, and Its Implication to the North China Craton Evolution. Master’s Thesis, China University of Geosciences, Beijing, China, 2012. (In Chinese with English abstract)
61. Xu, W.; Yang, D.; Pei, F.; Yu, Y. Petrogenesis of Fushan high-Mg# diorites from the southern Taihang Mts. in the central North Craton: Resulting from interaction of peridotite-melt derived from partial melting of delaminated lower continental crust. *Acta Petrol. Sin.* **2009**, *25*, 1947–1961. (In Chinese with English abstract).
62. Sun, Y. Petrogenesis and Mineralization of the Early Cretaceous Intrusive Rocks in Handan-Xingtai Area, Hebei Province, China. Ph.D. Thesis, China University of Geosciences, Wuhan, China, 2016. (In Chinese with English abstract).
63. Zheng, J.; Xie, G.; Liu, J.; Chen, M.; Wang, S.; Guo, S.; Gao, X.; Li, G. ⁴⁰Ar–³⁹Ar dating of phlogopite from the Xishimen skarn iron deposit in the Handan-Xingtai area, southern Hebei, and its implications. *Acta Petrol. Sin.* **2007**, *10*, 2513–2518. (In Chinese with English abstract)
64. Jiang, J.; Su, S.; Cui, X.; Liu, L.; Meng, W.; Wang, J. The processes and mechanism of lithospheric thinning in eastern North China Craton during Early Cretaceous: Evidence from Xishimen Complex, Hebei Province. *Acta Petrol. Sin.* **2020**, *36*, 356–390. (In Chinese with English abstract)
65. Jurek, K.; Hulínský, V. The use and accuracy of the ZAF correction procedure for the microanalysis of glasses. *Microchim. Acta.* **1980**, *73*, 183–198. [[CrossRef](#)]
66. Wang, F.; Ge, C.; Ning, S.; Nie, L.; Zhong, G.; White, N.C. A new approach to LA-ICP-MS mapping and application in geology. *Acta Petrol. Sin.* **2017**, *33*, 3422–3436. (In Chinese with English abstract)
67. Liu, Y.; Hu, Z.; Gao, S.; Günther, D.; Xu, J.; Gao, C.; Chen, H. In situ analysis of major and trace elements of anhydrous minerals by LA-ICP-MS without applying an internal standard. *Chem. Geol.* **2008**, *257*, 34–43. [[CrossRef](#)]
68. Zhang, J.; Liang, X.; Wang, F.; Wang, H.; Fan, Y.; Ba, T.; Meng, X. CorelKit: An Extensible CorelDraw VBA Program for Geoscience Drawing. *J. Earth Sci.* **2022**, 1–23. Available online: <https://kns.cnki.net/kcms/detail/42.1788.P.20221208.1416.002.html> (accessed on 15 December 2022).
69. Piccoli, P.M.; Candela, P.A.; Kohn, M.J.; Rakovan, J.; Hughes, J.M. Apatite in igneous systems. *Reviews in Mineralogy and Geochemistry. Rev. Mineral. Geochem.* **2002**, *48*, 255–292. Available online: <https://go.exlibris.link/mv7WkDtP> (accessed on 15 December 2022). [[CrossRef](#)]
70. Li, W.; Costa, F. A thermodynamic model for F–Cl–OH partitioning between silicate melts and apatite including non-ideal mixing with application to constraining melt volatile budgets. *Geochim. Cosmochim. Acta* **2019**, *269*, 203–222. [[CrossRef](#)]
71. Liu, J. Typomorphism and Significance of Apatite from the Granite in the Jiaodong and Xiaoqinling Regions. Master’s Thesis, China University of Geosciences, Beijing, China, 2020. (In Chinese with English abstract)
72. Sun, S.S.; McDonough, W.F. Chemical and isotopic systematic of oceanic basalts: Implications for mantle composition and processes. *Geol. Soc. Lond. Spec. Publ.* **1989**, *42*, 313–345. [[CrossRef](#)]
73. Zhang, J.; Li, S.; Wang, J.; Bai, M.; Lu, J.; Wei, H.; Nie, X.; Liu, H. The genetic mineralogical study of magnetite in Baijian and Xishimen skarn type of iron deposit, southern Hebei Province. *Earth Sci. Front.* **2013**, *20*, 76–87. (In Chinese with English abstract) [[CrossRef](#)]
74. Müntener, O.; Kelemen, P.B.; Grove, T.L. The role of H₂O during crystallization of primitive arc magmas under uppermost mantle conditions and genesis of igneous pyroxenites: An experimental study. *Contrib. Mineral. Petrol.* **2001**, *141*, 643–658. [[CrossRef](#)]

75. Chiaradia, M. Crustal thickness control on Sr/Y signatures of recent arc magmas: An Earth scale perspective. *Sci. Rep.* **2015**, *5*, 8115. [[CrossRef](#)]
76. Chiaradia, M.; Caricchi, L. Stochastic modelling of deep magmatic controls on porphyry copper deposit endowment. *Sci. Rep.* **2017**, *7*, 44523. [[CrossRef](#)]
77. Melekhova, E.; Blundy, J.; Robertson, R.; Humphreys, M.C.S. Experimental Evidence for Polybaric Differentiation of Primitive Arc Basalt beneath St. Vincent, Lesser Antilles. *J. Petrol.* **2015**, *56*, 161–192. [[CrossRef](#)]
78. Liang, X. Calculation of Oxygen Fugacity of Mesozoic Intrusive Rocks in Han–Xing Region, Southern Hebei Province and Their Geological Significances. Master’s Thesis, Hebei GEO University, Shijiazhuang, China, 2020. (In Chinese with English abstract)
79. Bai, F.; Jin, Y.; Fan, L.; Tang, Y.; Qin, C.; Zhang, J. Genetic mineralogical study of Ziquan diorite intrusion in the eastern of Handan-Xingtai region, Hebei province. *J. Hebei GEO Univ.* **2021**, *44*, 1–7, (In Chinese with English abstract).
80. Liang, X.; Zhang, J.; Lu, J.; Zhang, Q.; Wu, W.; Li, Q.; Bai, F.; Jin, Y.; Fan, L. Genetic mineralogy of apatite in Mesozoic intrusive rocks in the Handan-Xingtai Region, Hebei Province. *Geol. Explor.* **2020**, *56*, 969–984, (In Chinese with English abstract).
81. Xing, K.; Shu, Q. Applications of apatite in study of ore deposits: A review. *Miner. Depos.* **2021**, *40*, 189–205. (In Chinese with English abstract)
82. Burnham, A.D.; Berry, A.J. The effect of oxygen fugacity, melt composition, temperature and pressure on the oxidation state of cerium in silicate melts. *Chem. Geol.* **2014**, *366*, 52–60. [[CrossRef](#)]
83. Smythe, D.J.; Brenan, J.M. Cerium oxidation state in silicate melts: Combined fO₂, temperature and compositional effects. *Geochim. Cosmochim. Acta* **2015**, *170*, 173–187. [[CrossRef](#)]
84. Imai, A. Variation of Cl and SO₃ Contents of Microphenocrystic Apatite in Intermediate to Silicic Igneous Rocks of Cenozoic Japanese Island Arcs: Implications for Porphyry Cu Metallogenesis in the Western Pacific Island Arcs. *Resour. Geol.* **2004**, *54*, 357–372. [[CrossRef](#)]
85. Chelle-Michou, C.; Chiaradia, M. Amphibole and apatite insights into the evolution and mass balance of Cl and S in magmas associated with porphyry copper deposits. *Contrib. Mineral. Petrol.* **2017**, *172*, 105. [[CrossRef](#)]
86. Hsu, Y.; Zajacz, Z.; Ulmer, P.; Heinrich, C.A. Chlorine partitioning between granitic melt and H₂O-CO₂-NaCl fluids in the Earth’s upper crust and implications for magmatic-hydrothermal ore genesis. *Geochim. Cosmochim. Acta* **2019**, *261*, 171–190. [[CrossRef](#)]
87. Fan, L. The Study of Genetic Mineralogical of Amphibole in Mesozoic Intrusive Rocks in Han–Xing Area, Southern Hebei Province. Master’s Thesis, Hebei GEO University, Shijiazhuang, China, 2022. (In Chinese with English abstract)

Disclaimer/Publisher’s Note: The statements, opinions and data contained in all publications are solely those of the individual author(s) and contributor(s) and not of MDPI and/or the editor(s). MDPI and/or the editor(s) disclaim responsibility for any injury to people or property resulting from any ideas, methods, instructions or products referred to in the content.